FOURTH-ORDER FINITE DIFFERENCE ACOUSTIC LOGS IN A TRANSVERSELY ISOTROPIC FORMATION

by

N.Y. Cheng, C.H. Cheng, and M.N. Toksöz

Earth Resources Laboratory
Department of Earth, Atmospheric, and Planetary Sciences
Massachusetts Institute of Technology
Cambridge, MA 02139

ABSTRACT

In this paper we present a finite difference scheme for seismic wave propagation in a fluid-filled borehole in a transversely isotropic formation. The first-order hyperbolic differential equations are approximated explicitly on a staggered grid using an algorithm that is fourth-order accurate in space and second-order accurate in time. The grid dispersion and grid anisotropy are analyzed. Grid dispersion and anisotropy are well suppressed by a grid size of 10 points per wavelength. The stablility condition is also obtained from the dispersion analysis. This finite difference scheme is implemented on the nCUBE2 parallel computer with a grid decomposition algorithm. The finite difference synthetic waveforms are compared with those generated using the discrete wavenumber method. They are in good agreement. The damping layers effectively absorbed the boundary reflections. Four vertically heterogeneous borehole models: a horizontal layered formation, a borehole with a radius change, a semi-infinite borehole, and a semi-infinite borehole with a layer, are studied using the finite difference method. Snapshots from the finite difference results provide pictures of the radiating wavefields.

INTRODUCTION

Finite difference method is a very powerful technique in the modelling of seismic wave propagation in inhomogeneous media. There have been some applications of this method to acoustic logging problems. Stephen et al. (1985) directly applied the finite difference method to the second-order displacement formulation of the wave equation. The fluid-solid boundary at the borehole wall was treated explicitly. The velocity-stress finite difference method is widely used after Virieux's (1986) work. Kostek (1990), using the first order hyperbolic wave equation formulation, discretized on the staggered grid to solve the logging problem with a transducer in the borehole. Randall et al. (1991) al-

so used the velocity-stress finite difference formulation for the dipole acoustic logging problem. The azimuthal dependence of the wavefields is synthesized by Fourier transform. Randall (1991) extended the velocity-stress formulation to the nonaxisymmetric borehole problem. In the vertical wavenumber domain the finite difference algorithm is used in the horizontal plane. These finite difference schemes are second order accurate both in time and space. Levander (1988) investigated the fourth order finite difference method for the isotropic media in 2-D Cartesian coordinate. The fourth-order finite difference has less grid dispersion than the second-order one.

It is well-known that finely layered sedimentary rocks behave like a transversely isotropic solid and these layers are horizontal or nearly horizontal in the Earth. We can therefore assume that the symmetry axis of the transversely isotropic solid is vertical. For the problem of borehole wave propagation in a transversely isotropic formation the discrete wavenumber method is used (White and Tongtaow, 1981; Chan and Tsang, 1983; Schmitt, 1989). For an arbitrarily oriented transversely isotropic solid, Ellefsen et al. (1991) applied the pertubation method to study normal modes of a fluid-filled borehole. Leslie and Randall (1992) applied the finite difference method to the horizontal plane to calculate synthetic waveforms. All these methods depend on transforming the wave equation into the vertical wavenumber domain.

In this paper we formulate the wave propagation in a fluid-filled borehole surrounded by a transversely isotropic formation by the finite difference approximation. The finite difference equations are second order accurate in time and fourth order accurate in space. The stablility condition and grid dispersion are analyzed. The results of the finite difference method are also compared with those from the discrete wavenumber method. Four different vertically heterogeneous borehole models are studied.

FORMULATION

We consider a cylindrical fluid-filled borehole embedded in a transversely isotropic formation (Figure 1). In cylindrical coordinate (r, z), under the assumption of azimuthal symmetry, the equation of motion can be written as:

$$\rho \frac{\partial v_r}{\partial t} = \frac{\partial \sigma_{rr}}{\partial r} + \frac{\partial \sigma_{rz}}{\partial z} + \frac{\sigma_{rr} - \sigma_{\theta\theta}}{r} \qquad (1)$$

$$\rho \frac{\partial v_z}{\partial t} = \frac{\partial \sigma_{zz}}{\partial z} + \frac{\partial \sigma_{rz}}{\partial r} + \frac{\sigma_{rz}}{r} \qquad (2)$$

where v_r, v_z are the particle velocity in r and z directions, $\sigma_{rr}, \sigma_{\theta\theta}, \sigma_{zz}$ and σ_{rz} are stresses, ρ is the density. The time derivatives of the stress-strain relations for transversely isotropic media with symmetry axis along the z direction are:

$$\frac{\partial \sigma_{rr}}{\partial t} = c_{11} \frac{\partial v_r}{\partial r} + c_{12} \frac{v_r}{r} + c_{13} \frac{\partial v_z}{\partial z} \qquad (3)$$

$$\frac{\partial \sigma_{\theta\theta}}{\partial t} = c_{12}\frac{\partial v_r}{\partial r} + c_{12}\frac{v_r}{r} + c_{13}\frac{\partial v_z}{\partial z} \tag{4}$$

$$\frac{\partial \sigma_{zz}}{\partial t} = c_{13}\frac{\partial v_r}{\partial r} + c_{13}\frac{v_r}{r} + c_{33}\frac{\partial v_z}{\partial z} \tag{5}$$

$$\frac{\partial \sigma_{rz}}{\partial t} = c_{44}\frac{\partial v_r}{\partial z} + c_{44}\frac{\partial v_z}{\partial r} \tag{6}$$

where $c_{11}, c_{12}, c_{13}, c_{33}$ and c_{44} are elastic constants. $c_{66} = (c_{11} - c_{12})/2$. This first-order hyperbolic system of eqs. (1)–(6) can be approximated by explicit finite difference on a staggered grid (Figure 2). The finite difference equations for eqs. (1)–(6) are given in Appendix A. They are second-order accurate in time and fourth-order accurate in space. One advantage of this discretization is that we do not treat the fluid-solid boundary explicitly (Virieux 1986). We set the shear moduli to zero in the fluid as well as at the boundary. This is very useful for the fluid-filled borehole wave propagation problems.

To analyze grid dispersion we change to the Cartesian coordinate (x, z). This kind of analysis is very hard to do in the cylindrical coordinate system because of the r^{-1} terms. The grid dispersion in the cylindrical coordinate has similar properties as in the Cartesian coordinate. It is caused by the finite difference approximation to differentiation. First we consider plane wave propagation in a transversely isotropic media. The phase velocities of plane waves in transversely isotropic media have analytical expressions (Auld 1973). They are listed in Appendix B. There are three types of plane waves: pure shear, quasi-shear and quasi-p. Their velocities are angle dependent. Two types of transversely isotropic materials are used in this paper. They represent Mesaverde limestone and Green River shale (Thomsen, 1986). Their properties are listed in Tables 1 and 2, respectively. Their phase velocity surfaces are plotted in Figures 3 and 4. The shear wave anisotropy of Mesaverde limestone is about 5 percent and that of Green River shale is about 20 percent. The detailed grid dispersion analysis is given in Appendix B. The grid dispersions have closed form expression. The expressions are valid for fourth-order or second-order finite difference and transversely isotropic or isotropic. To simulate wave propagation in anisotropic media using finite difference we have to minimize the effects of the grid dispersion and grid anisotropy. For the Green River shale the grid dispersions are plotted against angle θ in Figures 5, 6 and 7 for pure shear, quasi-shear, and quasi-p wave, respectively. The quantity $\xi = 0.5$. Different H (grid size) values are considered. In the plots both fourth-order and second-order finite difference dispersions are shown. In the plots the grid dispersion and grid anisotropy are severe for the 3 points per wavelength grid size. For 10 points per wavelength the dispersion and anisotropy are very well suppressed in the fourth-order finite difference scheme.

The stability condition can also be obtained from the the dispersion analysis, which is given by (Appendix C):

$$\Delta t < \frac{\Delta z}{\sqrt{2}(|\eta_1| + |\eta_2|)V_{max}} \tag{7}$$

where $\eta_1 = \frac{8}{9}$ and $\eta_2 = -\frac{1}{24}$ are fourth order finite difference approximation coefficients. v_{max} is the maximum quasi-p wave velocity in the model. This condition is the same as the one given by Levander (1988), which is misprinted in the paper. For the second-order finite difference scheme where $\eta_1 = 1$ and $\eta_2 = 0$, this condition reduced the formula given by Virieux (1986).

This finite difference scheme is implemented on ERL's nCUBE2 MIMD parallel computer with a grid decomposition algorithm. This algorithm decomposes the whole grid into small subgrids and then maps these subgrids into nodes. The finite difference algorithm is calculated on each subgrid. Subgrid boundary values are communicated between nearby nodes.

COMPARISON WITH DISCRETE WAVENUMBER METHOD

To check the results obtained by the fourth-order finite difference scheme, we compare them with the discrete wavenumber technique. We consider a fluid-filled borehole with a radius of 0.1 m. Acoustic velocity of the borehole fluid is 1500 m/s and density is 1.0 g/cc. To do the finite difference calculation we chose $\Delta z = \Delta r = 1$cm and $\Delta t = 0.001$ms. A grid size of 256×512 is used. To absorb the boundary reflections we put a 50 point sponge layer around the outside of the boundary. The source-receiver separation is 2 m. They are both located at the center of the borehole. A point compressional Kelly source (Stephen et al., 1985) is applied at the origin. The Kelly source is used throughout this paper.

First, we consider the weakly anisotropic Mesaverde limestone formation. The comparison of finite difference synthetic waveform and discrete wavenumber calculation is plotted in Figure 8. The source center frequency is 8 kHz. The plot shows good agreement between two methods. The damping layer did a very good job of absorbing the boundary reflections. Finite difference synthetics with different source-receiver distances are plotted in Figure 9. Figure 10 shows the waveforms of the radial stress σ_{rr} recorded outside of the borehole. It shows the two body wave arrivals. The snapshot of the σ_{rr} wavefield at time 0.6 ms is plotted in Figure 11. The radiation patterns of the body waves can be easily observed from the plot. In this weak anisotropy case the wavefront is close to a circle.

Next we consider the Green River shale formation as a moderately anisotropic formation. The comparison of the finite difference waveform and discrete wavenumber method is shown in Figure 12. The source center frequency is 10 kHz. Once again there is good agreement between two methods. Twelve traces of waveforms at the center of borehole are plotted in the Figure 13 and waveforms recorded outside of the borehole are plotted in Figure 14. Because of the anisotropy the waveforms outside of the borehole are more complicated than in the isotropic case. A snapshot of the wavefield at time 0.8

ms is shown in Figure 15. The wavefront becomes elliptic due to the anisotropy. Also, shear wave splitting can be observed from the snapshot.

VERTICALLY HETEROGENEOUS BOREHOLE MODELS

We apply the finite difference method to simulate wave propagation in the fluid-filled borehole with vertical heterogeneity.

Borehole With Radius Change

First we consider a sharp borehole radius change. The borehole radius changes from 0.15 m to 0.1 m at $z = 2.0$ m. The receiver array is located in the center of the borehole. The distance from the source to the first receiver is 1 m and the separation between receivers is 0.1 m. A source with center frequency 4 kHz is located at the origin. The finite difference synthetics are plotted in Figure 16. A strong Stoneley wave reflection is generated from the borehole radius change. The snapshot of the wavefield is shown in Figure 17. The snapshot shows the incident Stoneley wave passed the radius change. The reflected Stoneley wave travels upward. There are also body waves radiated into the formation from the radius change. These body waves are interfering with waves from the origin source radiations.

Borehole with Horizontal Layers

Next we consider a fluid-filled borehole surrounded by a formation which has two horizontal layers. Layer 1 is Green River shale and layer 2 is Mesaverde limestone. The layer boundary is located at $z = 2.0$ m. The source and receiver array have the same configuration as in the previous model. The finite difference synthetics are plotted in Figure 18. The plot shows little effect of the horizontal layer on Stoneley wave propagation. There is a subtle change of the Stoneley wave velocity in the Mesaverde limestone layer because the shear wave velocity of the Mesaverde limestone is much higher than that of the Green River shale. The snapshots of the wavefield of σ_{rr} at time 1.7 ms and 2.1 ms represent the time when the Stoneley waves hit and pass the layer boundary (Figure 19). The layer boundary only causes very small reflections.

Semi-Infinite Borehole Model

We next consider a semi-infinite, fluid-filled borehole terminated at $z = 2.5$ m. The formation is Green River shale. The source is a vertical ring force applied at $r = 0.05$

m on the bottom of the borehole. This is similar to a Survey While Drilling (SWD) situation. The source center frequency is 8 kHz. The receiver array is located at $r = 1.0$ m and the first receiver started at $z = 0.6$ m with receivers separated by 0.1 m. The finite difference synthetics are plotted in Figure 20 and the snapshot in Figure 21. The vertical ring force generates body waves and guided waves inside the borehole, but inside the formation the borehole effect is mostly near the borehole. This is very clear from the snapshot. The wavefront becomes elliptic due to the anisotropy.

Semi-Infinite Borehole With A Layer

From the borehole model discussed above we added another horizontal layer to the model. The layer of Mesaverde limestone is put at $z = 3.0$ m. The source and the receiver array are the same as above. The synthetics are plotted in Figure 22. Compared with Figure 20, the waveforms received by the receivers in the Green River shale are almost the same. The waveforms received by the receiver in the Mesaverde limestone have early quasi-P wave arrivals. The snapshot is shown in Figure 23. We see only a small reflection from the layer boundary. Most of the energy is transmitted into the Mesaverde limestone. The wavefront is close to circular because Mesaverde limestone only has about 5% anisotropy.

CONCLUSIONS

The fourth-order finite difference scheme provides a reliable full wave solution to borehole wave propagation in the transversely isotropic formation with vertical heterogeneity. The results of the finite difference scheme are in good agreement with the discrete wavenumber method. When implemented on the nCUBE2 parallel computer this scheme provides a real time picture of wave propagation. The wavefield snapshots provide radiation patterns for infinite and semi-infinite boreholes in transversely isotropic formations.

ACKNOWLEDGEMENTS

REFERENCES

Auld, B.A., 1973, Acoustic Fields and Waves in Solids, Vol.1, *John Wiley & Sons, Inc.*

Chan, A.K., and Tsang, L., 1983, Propagation of acoustic waves in a fluid-filled borehole surrounded by a concentrically layered transversely isotropic formation; *J. Acoust. Soc. Am., 74,* 1605–1616.

Ellefsen, K.J., Cheng, C.H., and Toksöz, M.N., 1991, Applications of pertubation theory to acoustic logging; *J. Geophys. Res., 96,* 537–549.

Kostek, S., 1990, Modelling of elastic wave propagation in a fluid-filled borehole excited by a piezoelectric transducer; Masters Thesis, Massachusetts Institute of Technology, Cambridge, Mass.

Leslie, H.D., and Randall, C.T., 1992, Multipole sources in boreholes penetrating anisotropic formations: numerical and experimental results; *J. Acoust. Soc. Am., 91,* 12–27.

Levander, A.R., 1988, Fourth-order finite-difference P-SV seismograms *Geophysics, 53,* 1425–1436.

Randall, C.T., 1991, Multipole acoustic waveforms in nonaxisymmetric boreholes and formations; *J. Acoust. Soc. Am., 90,* 1620–1631.

Randall, C.T., Scheibner, D.J., and Wu, P.T., 1991, Multipole borehole acoustic waveforms: synthetic logs with beds and borehole washouts; *Geophysics, 56,* 1757–1769.

Schmitt, D.P., 1989, Acoustic multipole logging in transversely isotropic poroelastic formations; *J. Acoust. Soc. Am., 86,* 2397–2421.

Stephen, R.A., Pardo-Casas, F., and Cheng, C.H., 1985, Finite-difference synthetic acoustic logs; *Geophysics 50,* 1588–1609.

Thomsen, L., 1986, Weak elastic anisotropy; *Geophysics, 51,* 1954–1966.

Virieux, J., 1986, P-SV wave propagation in heterogeneous media: velocity-stress finite-difference method; *Geophysics, 51,* 889–901.

White, J.E., and Tongtaow, C., 1981, Cylindrical waves in transversely isotropic media; *J. Acoust. Soc. Am., 70,* 1147–1155.

APPENDIX A

Finite Difference Equations

We discretize the cylindrical coordinate (r, z) and time t on the staggered grids, assuming that $r = m\Delta r$ or $r = (m \pm \frac{1}{2})\Delta r$, $z = n\Delta z$ or $z = (n \pm \frac{1}{2})\Delta z$, and $t = l\Delta t$ or $t = (l \pm \frac{1}{2})\Delta t$.

Let us define the second order forward difference operator in time D_t^+:

$$D_t^+ f_j = \frac{f_{j+1} - f_j}{\Delta t}; \qquad (A.1)$$

the forward average operator A_r^+:

$$A_r^+ f_j = \frac{f_{j+1} + f_j}{2r}; \qquad (A.2)$$

and the fourth order forward difference operator in space D^+:

$$D^+ f_j = \gamma_1(f_{j+1} - f_j) + \gamma_2(f_{j+2} - f_{j-1}); \qquad (A.3)$$

where for r coordinate $\gamma_1 = \frac{9}{8\Delta r}$, $\gamma_2 = \frac{-1}{24\Delta r}$ and for z coordinate $\gamma_1 = \frac{9}{8\Delta z}$, $\gamma_2 = \frac{-1}{24\Delta z}$.

The finite difference approximations for equations $(1) - (6)$ can be written as:

$$D_t^+ v_r(m, n + \frac{1}{2}, l - \frac{1}{2}) = (D_r^+ \sigma_{rr}(m - \frac{1}{2}, n - \frac{1}{2}, l) + D_z^+ \sigma_{rz}(m, n, l)$$

$$+ A_r^+(\sigma_{rr}(m - \frac{1}{2}, n + \frac{1}{2}, l) + \sigma_{\theta\theta}(m - \frac{1}{2}, n + \frac{1}{2}, l)))/\rho(m, n + \frac{1}{2}) \quad (A.4)$$

$$D_t^+ v_z(m + \frac{1}{2}, n, l - \frac{1}{2}) = (D_z^+ \sigma_{zz}(m - \frac{1}{2}, n - \frac{1}{2}, l) + D_r^+ \sigma_{rz}(m, n, l)$$

$$+ A_r^+ \sigma_{rz}(m, n, l))/\rho(m + \frac{1}{2}, n) \quad (A.5)$$

$$D_t^+ \sigma_{rr}(m + \frac{1}{2}, n + \frac{1}{2}, l) = c_{11}(m + \frac{1}{2}, n + \frac{1}{2})D_r^+ v_r(m, n + \frac{1}{2}, l + \frac{1}{2})$$

$$+ c_{12}(m + \frac{1}{2}, n + \frac{1}{2})A_r^+ v_r(m, n + \frac{1}{2}, l + \frac{1}{2})$$

$$+ c_{13}(m + \frac{1}{2}, n + \frac{1}{2})D_z^+ v_z(m + \frac{1}{2}, n, l + \frac{1}{2}) \quad (A.6)$$

$$D_t^+ \sigma_{\theta\theta}(m + \frac{1}{2}, n + \frac{1}{2}, l) = c_{12}(m + \frac{1}{2}, n + \frac{1}{2})D_r^+ v_r(m, n + \frac{1}{2}, l + \frac{1}{2})$$

$$+ c_{11}(m + \frac{1}{2}, n + \frac{1}{2})A_r^+ v_r(m, n + \frac{1}{2}, l + \frac{1}{2})$$

$$+ c_{13}(m + \frac{1}{2}, n + \frac{1}{2})D_z^+ v_z(m + \frac{1}{2}, n, l + \frac{1}{2}) \quad \text{(A.7)}$$

$$D_t^+ \sigma_{zz}(m + \frac{1}{2}, n + \frac{1}{2}, l) = c_{13}(m + \frac{1}{2}, n + \frac{1}{2})D_r^+ v_r(m, n + \frac{1}{2}, l + \frac{1}{2})$$

$$+ c_{13}(m + \frac{1}{2}, n + \frac{1}{2})A_r^+ v_r(m, n + \frac{1}{2}, l + \frac{1}{2})$$

$$+ c_{33}(m + \frac{1}{2}, n + \frac{1}{2})D_z^+ v_z(m + \frac{1}{2}, n, l + \frac{1}{2}) \quad \text{(A.8)}$$

$$D_t^+ \sigma_{rz}(m, n, l) = c_{44}(m, n)(D_r^+ v_z(m, n - \frac{1}{2}, l + \frac{1}{2}) + D_z^+ v_r(m - \frac{1}{2}, n, l + \frac{1}{2})). \quad \text{(A.9)}$$

APPENDIX B

Phase Velocity Surfaces and Grid Dispersions

In this appendix we give the expressions for the phase velocity surfaces and grid dispersion relations in the Cartesian coordinate (x, z).

For a transversely isotropic medium with its symmetry along the z axis, the solution of the Christoffel equation has an analytical expression (Auld 1973). The phase velocity of the pure shear wave is given by:

$$V_s(\theta) = \sqrt{\frac{c_{66}sin^2\theta + c_{44}cos^2\theta}{\rho}} \tag{B.1}$$

the phase velocity of the quasi-shear wave is:

$$V_{qS}(\theta) = \sqrt{\frac{c_{11}sin^2\theta + c_{33}cos^2\theta + c_{44} - \sqrt{D}}{2\rho}} \tag{B.2}$$

and the phase velocity of the quasi-p wave is:

$$V_{qP}(\theta) = \sqrt{\frac{c_{11}sin^2\theta + c_{33}cos^2\theta + c_{44} + \sqrt{D}}{2\rho}} \tag{B.3}$$

where

$$D = [(c_{11} - c_{44})sin^2\theta + (c_{44} - c_{33})cos^2\theta]^2 + (c_{13} + c_{44})^2sin^22\theta \tag{B.4}$$

and θ is the angle measured from the z axis.

For grid dispersion analysis consider a plane wave with wavelength λ, which makes an angle θ with the z axis. Define quantity ξ as:

$$\xi = V\frac{\Delta t}{\Delta z} \tag{B.5}$$

where $V = \sqrt{\frac{c_{11}}{\rho}}$ and assuming $\Delta x = \Delta z$. Define quantity H as :

$$H = \frac{\Delta z}{\lambda} \qquad (B.6)$$

H measures the numerical sample rate per wavelength and ξ measures the numerical dispersion of the finite difference approximation. Introduce q as the ratio of numerical phase velocity to true phase velocity. This nondimensional velocity q for the pure shear wave is:

$$q_s = \frac{V}{\pi \xi H V_s(\theta)} sin^{-1}(\frac{\xi V_s(\theta)}{V} \sqrt{A_x^2 + A_z^2}); \qquad (B.7)$$

for the quasi-shear wave is:

$$q_{qS} = \frac{V}{\pi \xi H V_{qS}(\theta)} sin^{-1}(\frac{\xi V_{qS}(\theta)}{V} \sqrt{A_x^2 + A_z^2}); \qquad (B.8)$$

and for the quasi-p wave is

$$q_{qP} = \frac{V}{\pi \xi H V_{qP}(\theta)} sin^{-1}(\frac{\xi V_{qP}(\theta)}{V} \sqrt{A_x^2 + A_z^2}); \qquad (B.9)$$

where

$$A_x = \eta_1 sin(\pi H cos\theta) + \eta_2 sin(3\pi H cos\theta) \qquad (B.10)$$

$$A_z = \eta_1 sin(\pi H sin\theta) + \eta_2 sin(3\pi H sin\theta) \qquad (B.11)$$

and η_1, η_2 are constants. For fourth order finite difference in space $\eta_1 = \frac{9}{8}$ and $\eta_2 = -\frac{1}{24}$. For second order $\eta_1 = 1$ and $\eta_2 = 0$. In isotropic media and the second order finite difference case, equations (B.7) and (B.9) reduce to the same forms of dispersion relations given by Virieux (1986).

APPENDIX C

Stable Condition

Following Appendix B, the stable condition can be obtained by setting the argument of inverse sine function in equation (B.9) to less than 1. Assuming V_{max} is the maximum quasi-p velocity in the model, the condition is:

$$\frac{\Delta t}{\Delta z} V_{max} \sqrt{A_x^2 + A_z^2} < 1 \qquad (C.1)$$

It is easy to verify numerically that:

$$\sqrt{A_x^2 + A_z^2} < \sqrt{2}(|\eta_1| + |\eta_2|). \qquad (C.2)$$

So the stable condition is:

$$\Delta t < \frac{\Delta z}{\sqrt{2}(|\eta_1| + |\eta_2|)V_{max}} \qquad (C.3)$$

Quantity	Value
c_{11}	7.23×10^{10} Pa
c_{13}	2.06×10^{10} Pa
c_{33}	6.50×10^{10} Pa
c_{44}	2.21×10^{10} Pa
c_{66}	2.51×10^{10} Pa
ρ	2500 kg/m^3

Table 1: Transversely isotropic model 1. The symmetry axis is parallel to the z axis. It represents Mesaverde limestone (Thomsen 1986).

Quantity	Value
c_{11}	3.126×10^{10} Pa
c_{13}	0.245×10^{10} Pa
c_{33}	2.249×10^{10} Pa
c_{44}	0.649×10^{10} Pa
c_{66}	0.882×10^{10} Pa
ρ	2075 kg/m^3

Table 2: Transversely isotropic model 2. The symmetry axis is parallel to the z axis. It represents Green River shale (Thomsen 1986).

Cheng et al.

Source

Fluid

Transversely Isotropic Formation

Absorbing Boundary

Absorbing Boundary

r

z
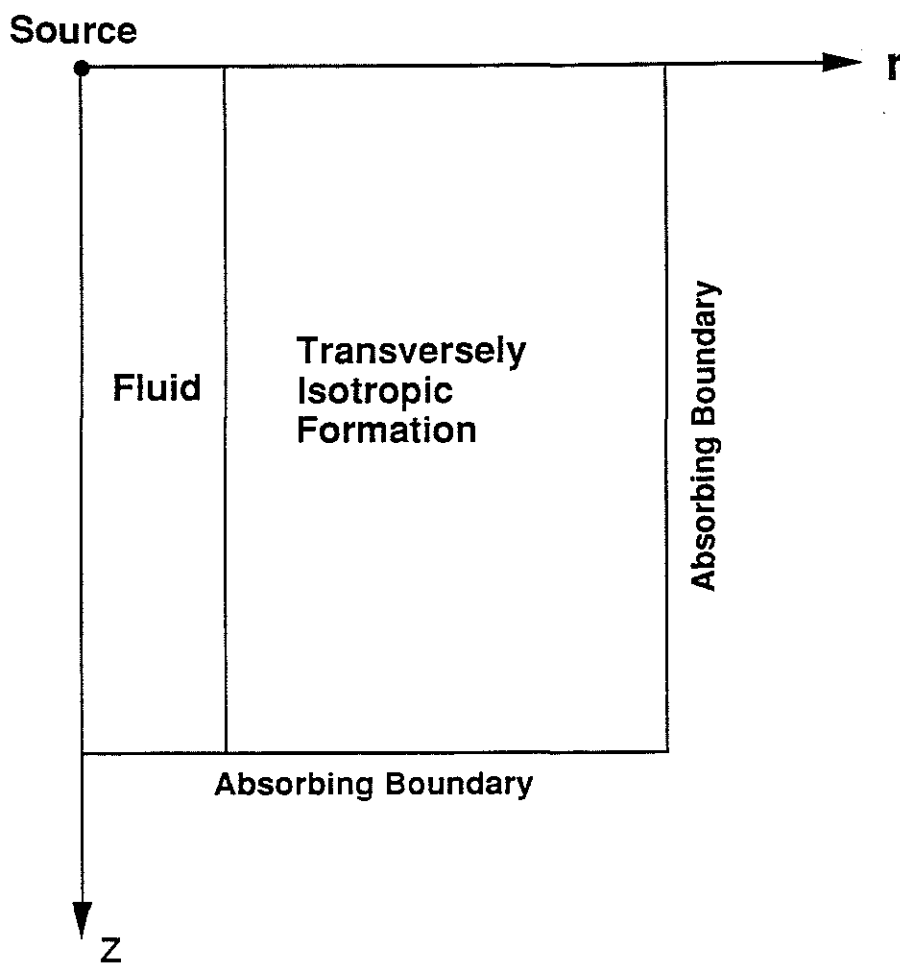
Figure 1: Borehole geometry used for the finite difference method. A source located at the origin. The r axis and z axis are also the symmetry axes.
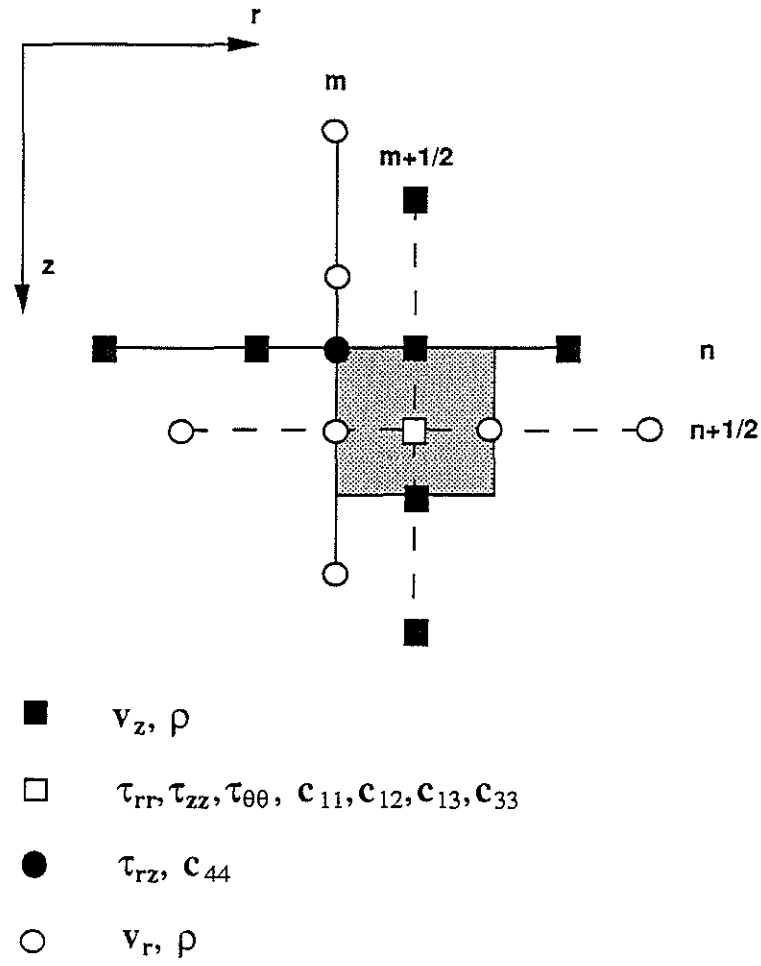
Figure 2: Discretization of the first order hyperbolic equations on a staggered grid using fourth-order finite difference approximation. It shows the field variables and elastic constants on the grid.
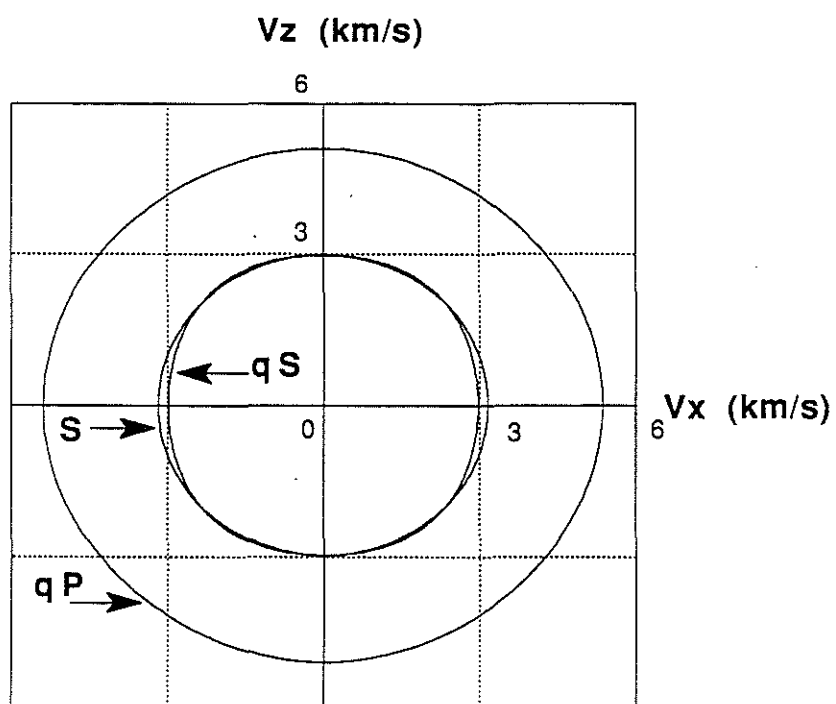
Figure 3: Phase velocity surfaces in the $x - z$ plane for pure shear, quasi-shear and quasi-p waves in Mesaverde limestone.
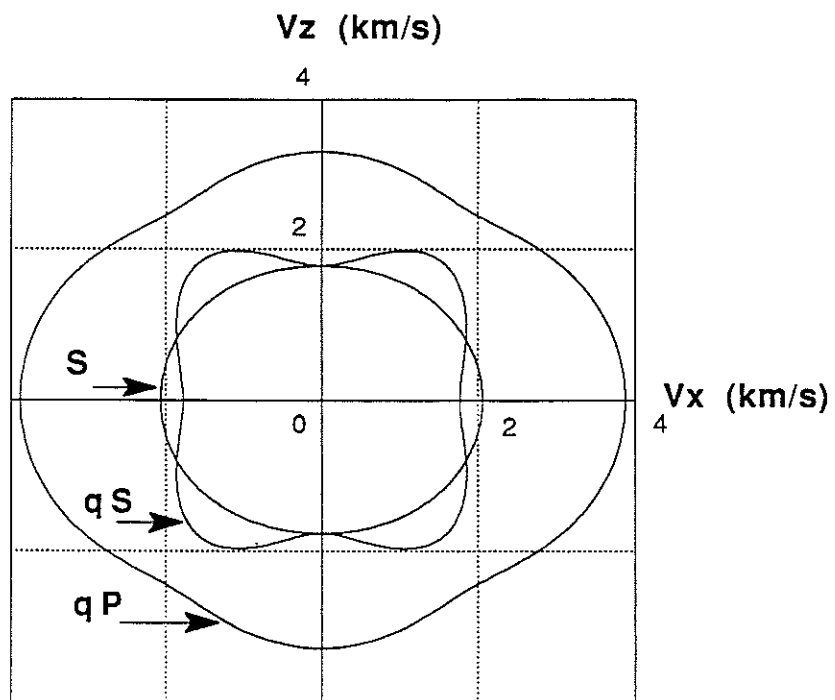
Figure 4: Phase velocity surfaces in the $x - z$ plane for pure shear, quasi-shear and quasi-p waves in Green river shale.

Cheng et al.
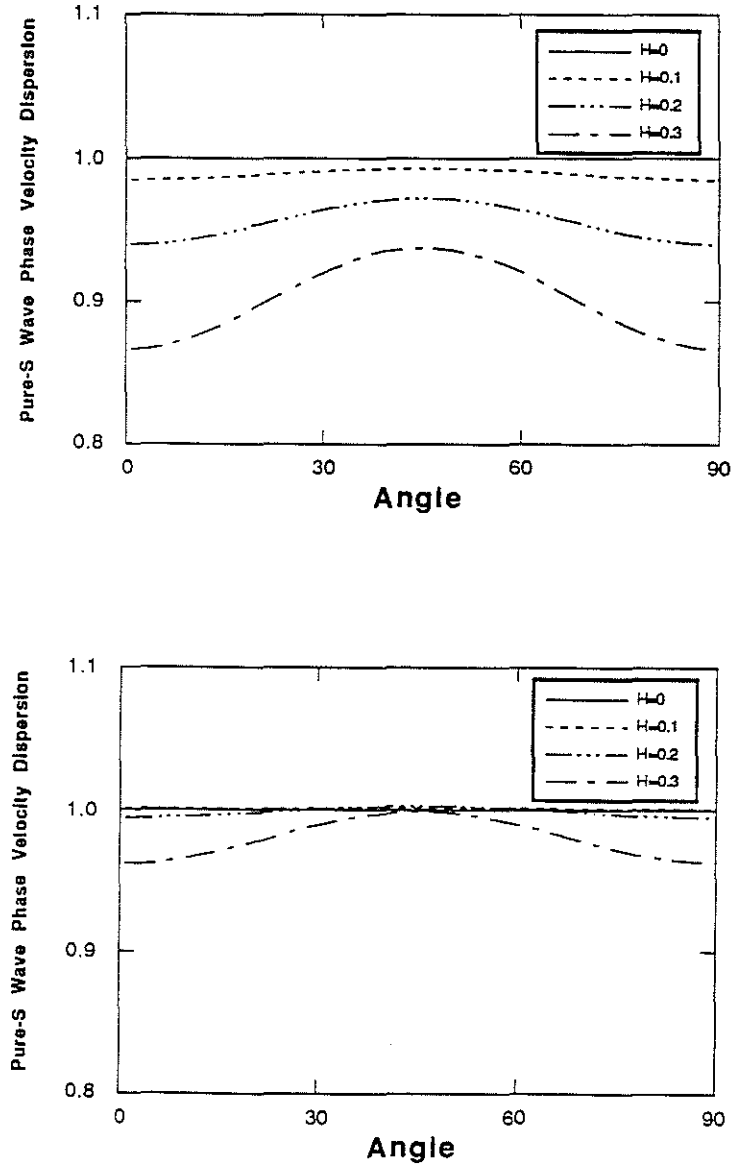
Figure 5: Pure shear wave grid dispersion versus plane wave incident angle for different
   H values. $\xi = 0.5$. Numerical velocity is normalized with the true velocity. Second-
   order finite difference (above). Fourth-order finite difference (below).
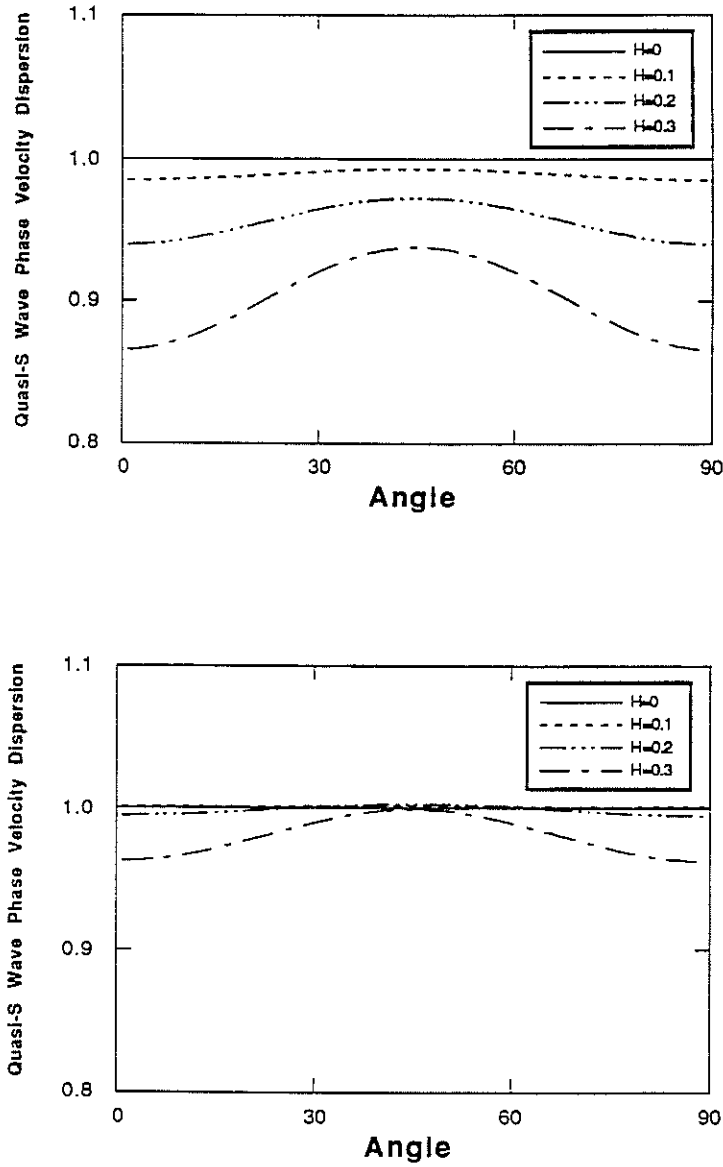
Figure 6: Quasi-shear wave grid dispersion versus plane wave incident angle for different H values. $\xi = 0.5$. Numerical velocity is normalized with the true velocity. Second-order finite difference (above). Fourth-order finite difference (below).
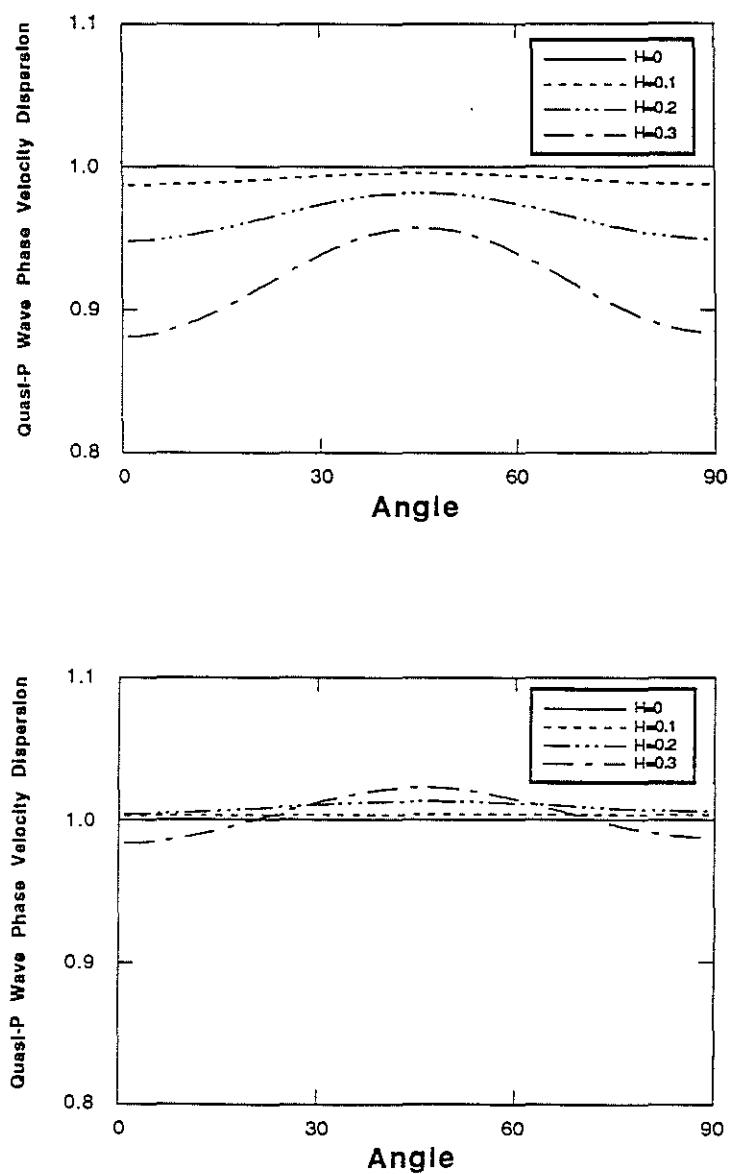
Figure 7: Quasi-P wave grid dispersion versus plane wave incident angle for different H values. $\xi = 0.5$. Numerical velocity is normalized with the true velocity. Second-order finite difference (above). Fourth-order finite difference (below).
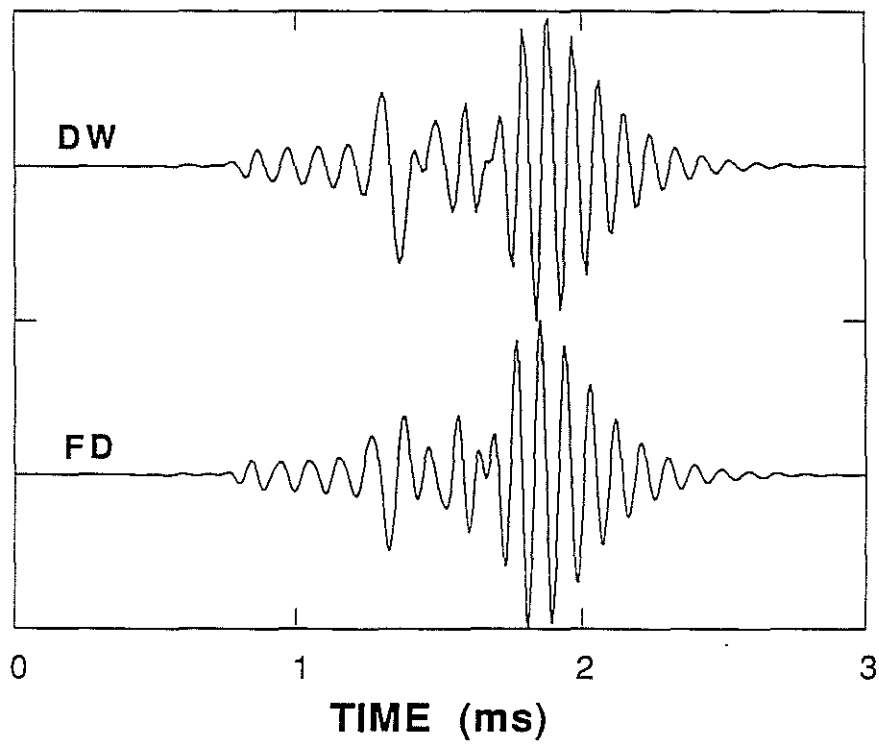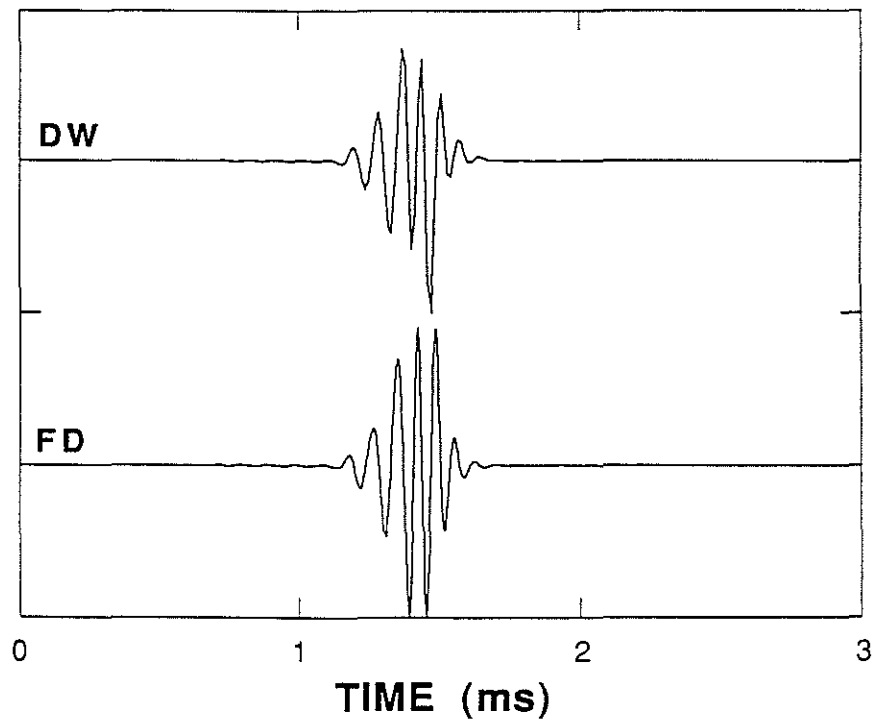
Figure 8: Comparison of finite difference (FD) synthetic waveform with the discrete wavenumber method (DW) for Mesaverde limestone. The separation of source-receiver is 2 m. The center frequency of Kelly source is 8 kHz.
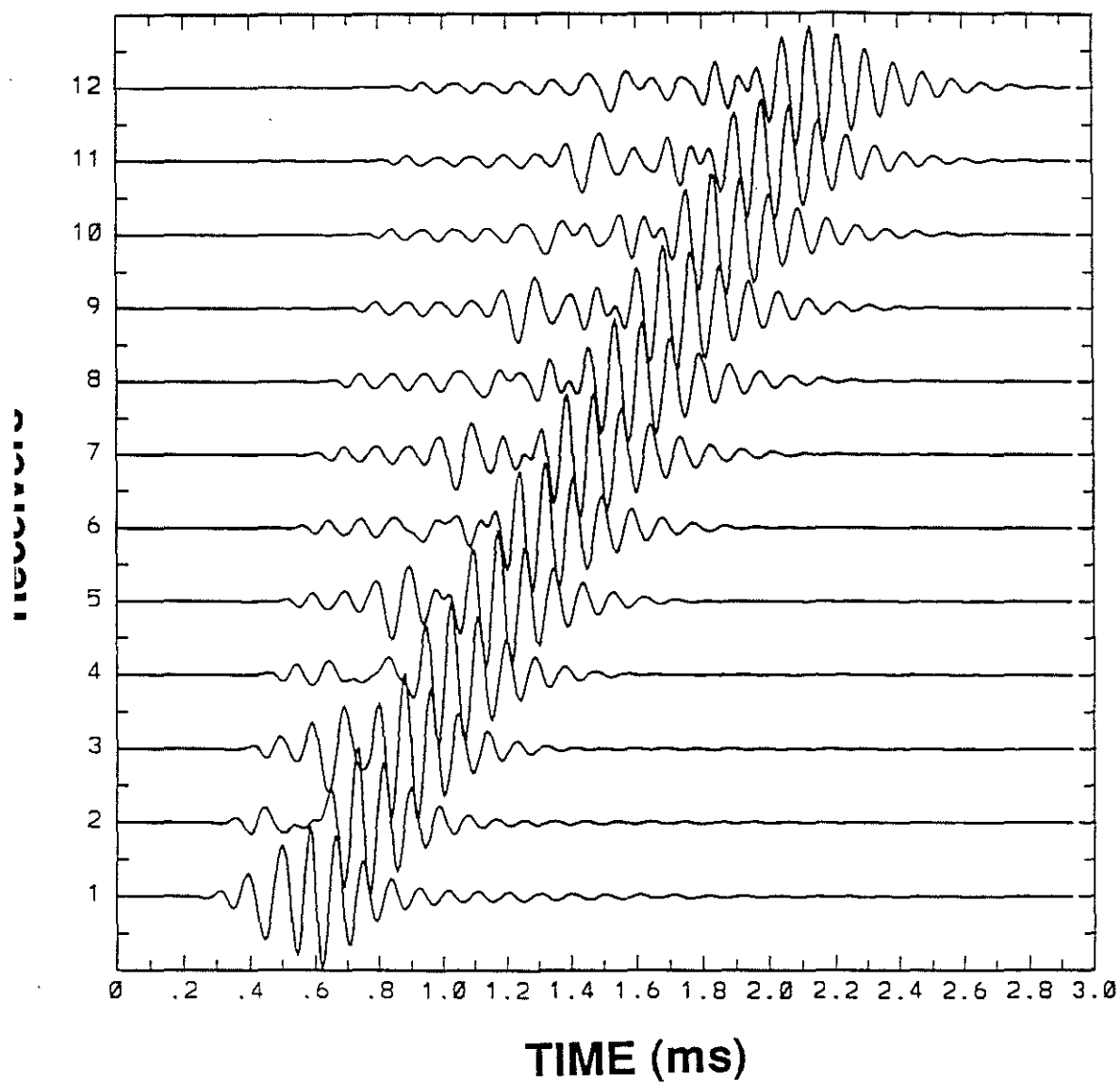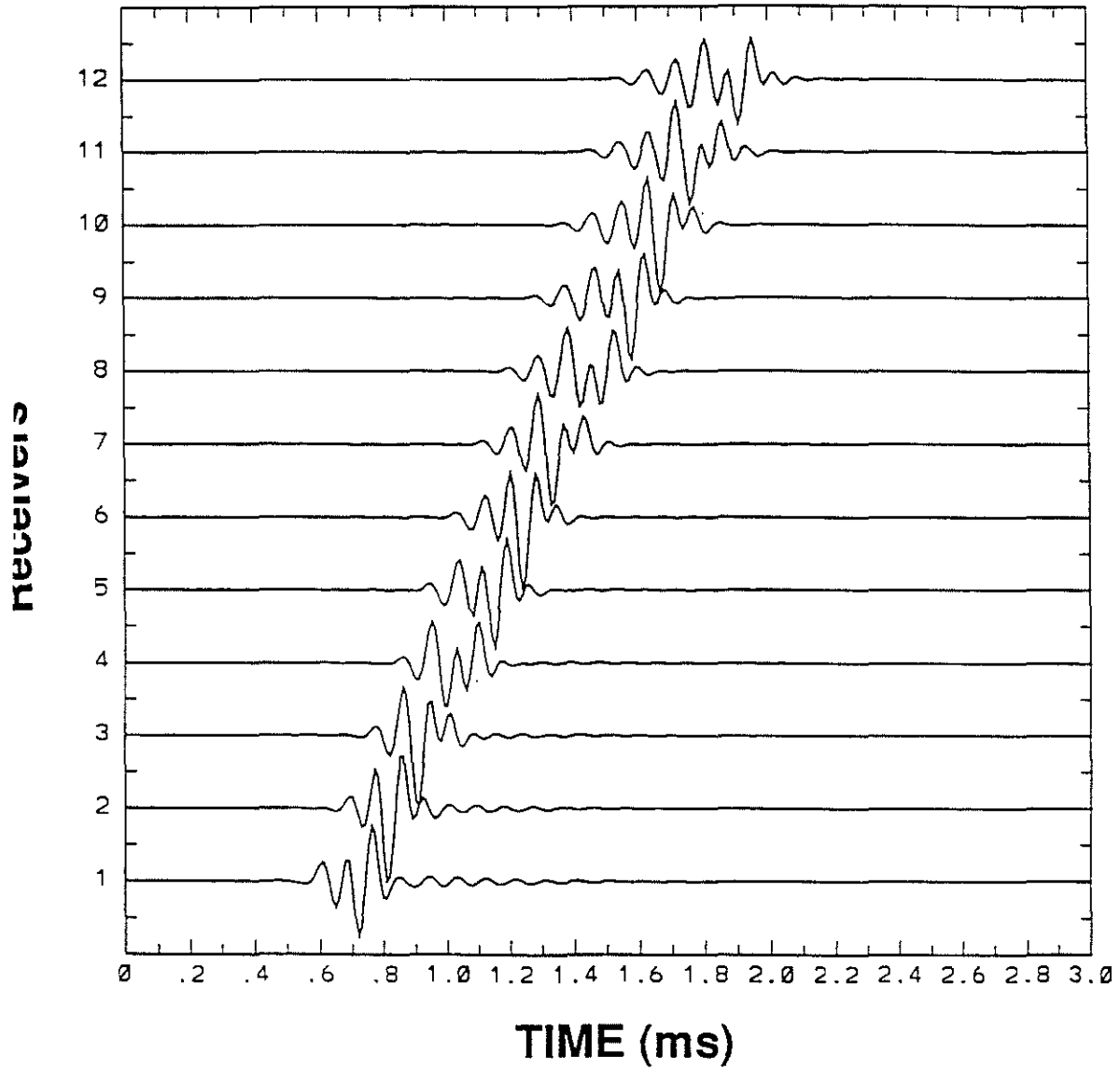
Figure 9: Finite difference synthetics in the center of the borehole with Mesaverde limestone formation. The separation of the source and the first receiver is 1 m. The spacing between receivers is 0.15 m. The center frequency of Kelly source is 8 kHz.
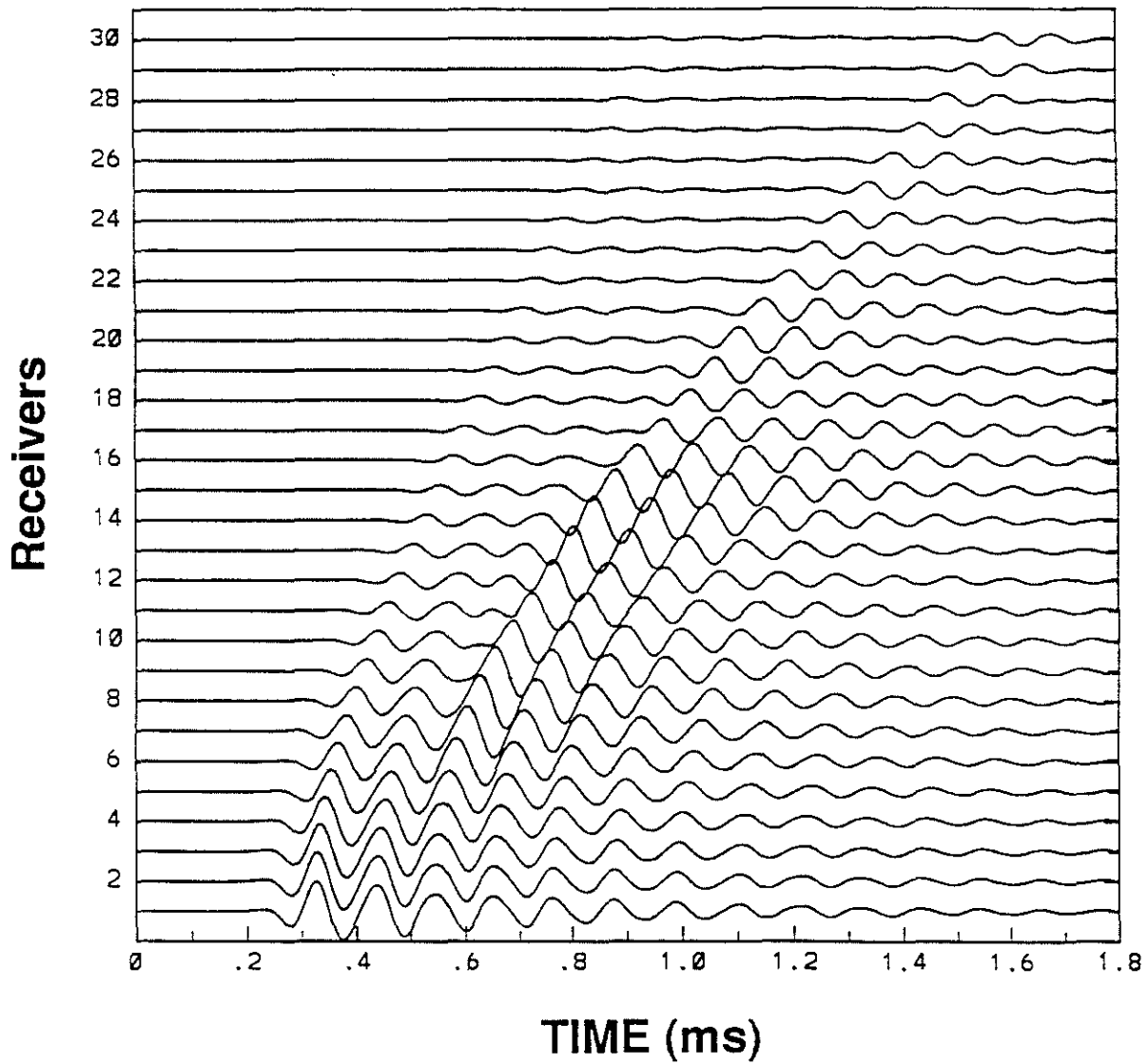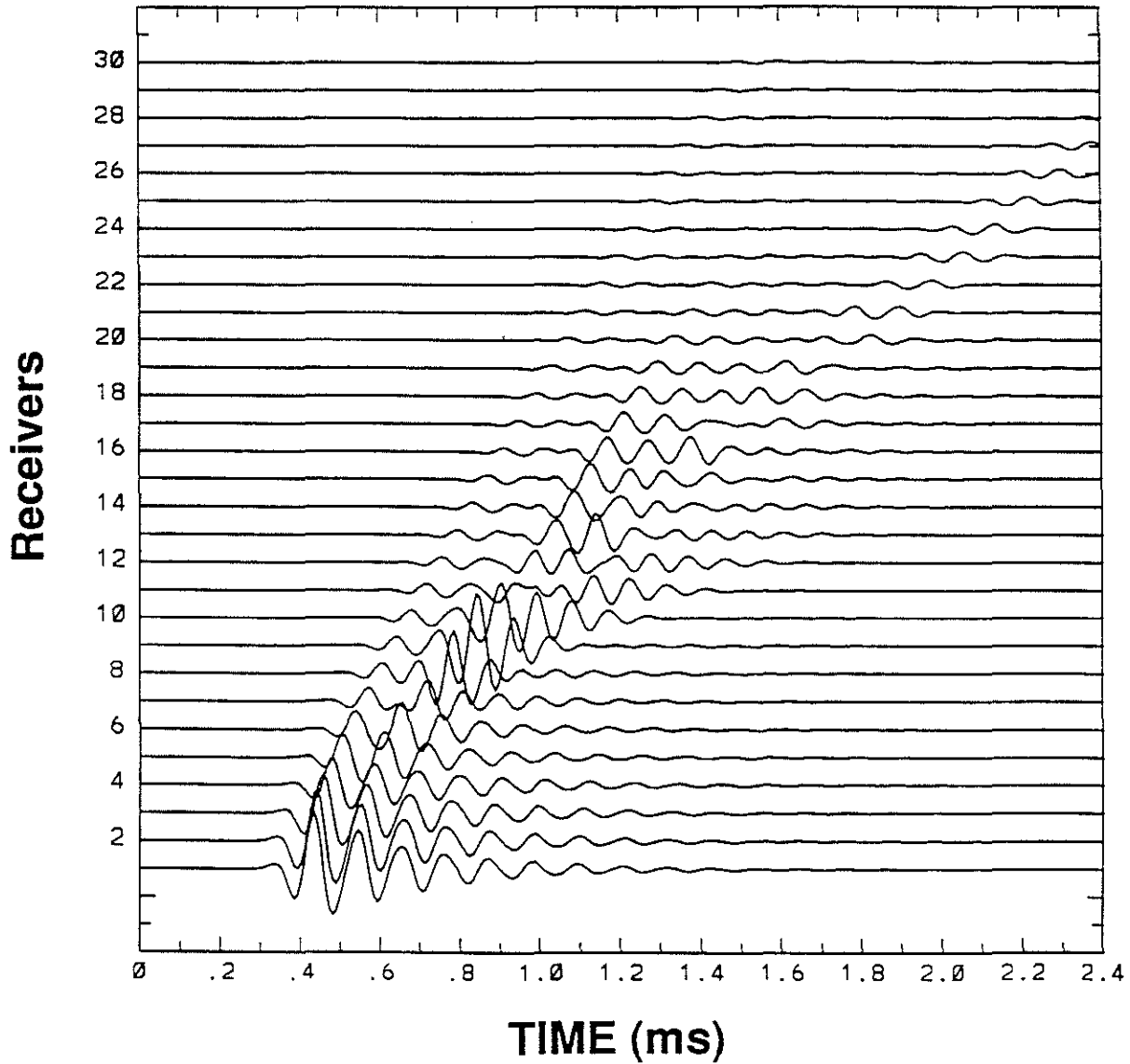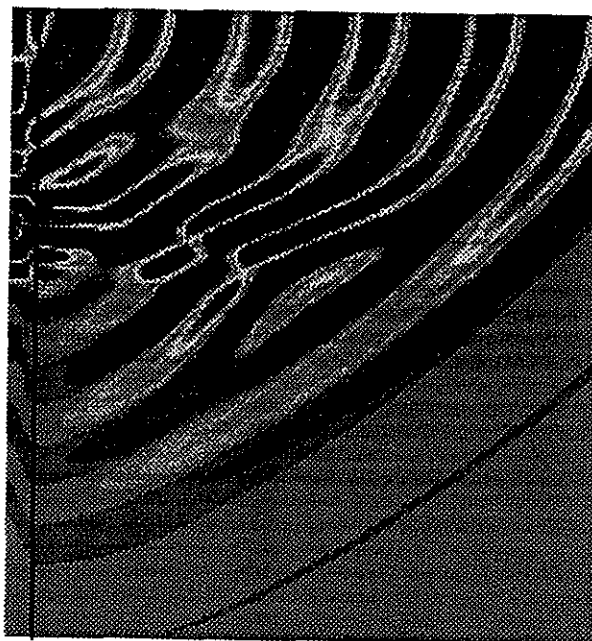
Figure 10: Finite difference synthetics outside of the borehole 1.5 m for Mesaverde limestone. The Source located at the origin with 8 kHz center frequency Kelly source. The receivers started at $z = 0$ with separation 0.15 m and recorded σ_{rr}.

Source

Borehole
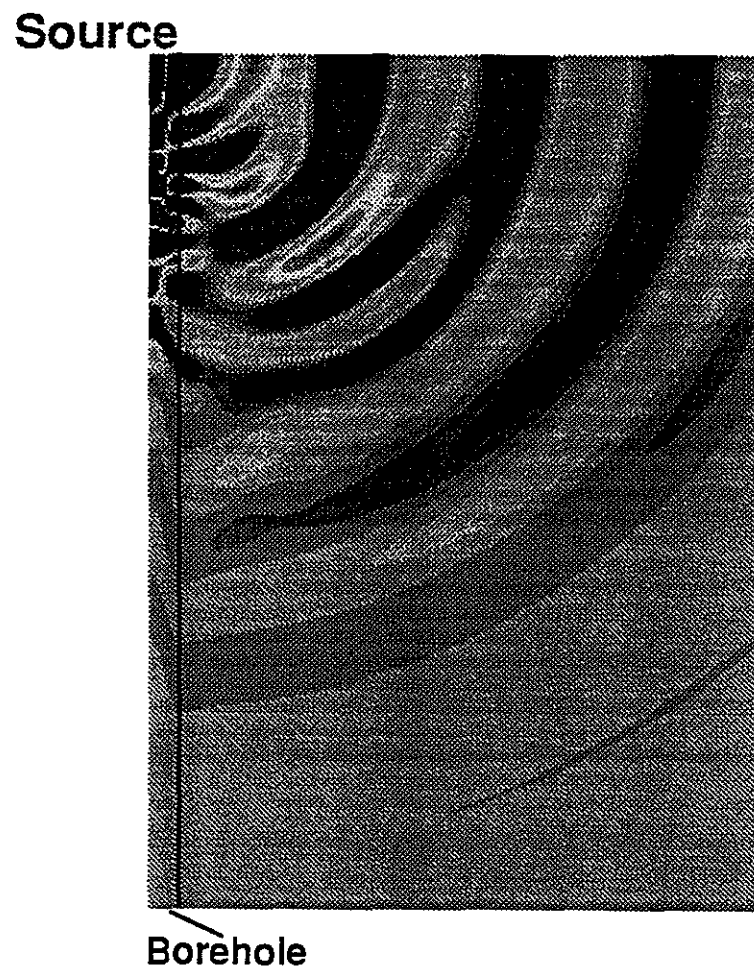
Figure 11: Snapshot of wavefield σ_{rr} from finite difference simulation for Mesaverde limestone at time 0.6 ms.

Figure 12: Comparison of finite difference (FD) synthetic waveform with discrete wavenumber method (DW) for Green River shale. The separation of source-receiver is 2 m. The center frequency of Kelly source is 10 kHz.

Figure 13: Finite difference synthetics in the center of the borehole for Green River shale. The separation of the source and the first receiver is 1 m. The spacing between receivers is 0.15 m. The center frequency of Kelly source is 10 kHz.

Figure 14: Finite difference synthetics outside of the borehole 1.5 m for Green River shale with a 10 kHz center frequency Kelly source. The source is located at the origin. The receivers started at $z = 0$ with separation 0.15 m and recorded σ_{rr}.

Cheng et al.

Source

Borehole

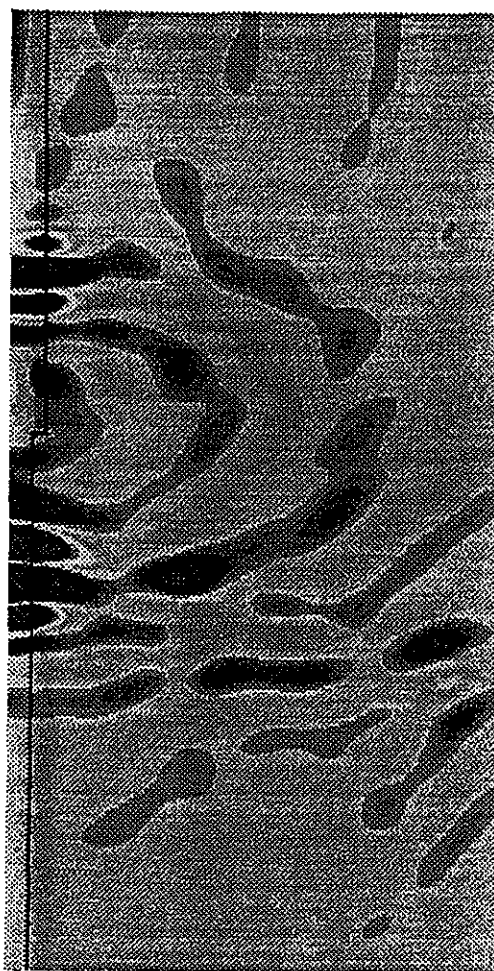Figure 15: Snapshot of wavefield σ_{rr} from finite difference simulation for Green River shale at time 0.8 ms.
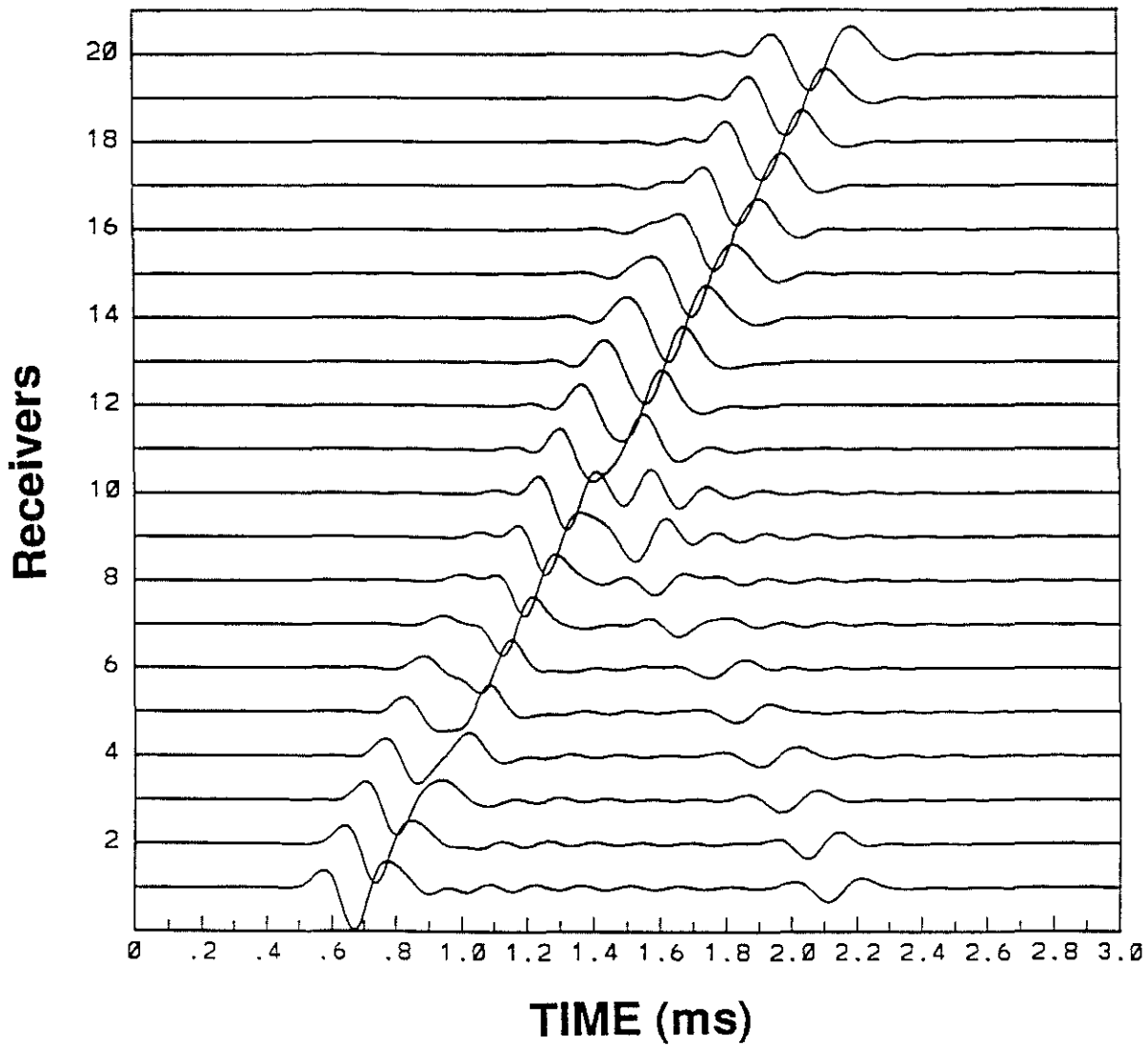
Figure 16: Finite difference synthetics at the center of the borehole with source center frequency at 4 kHz. The receivers start at $z = 1.0$ m and receiver separation is 0.1 m. The borehole radius changed from 0.15 m to 0.1 m at $z = 2.0$ m and the formation is Green River shale.

Source

Borehole

Figure 17: Snapshot of wavefield σ_{rr} for borehole radius change model at time 2.2 ms.
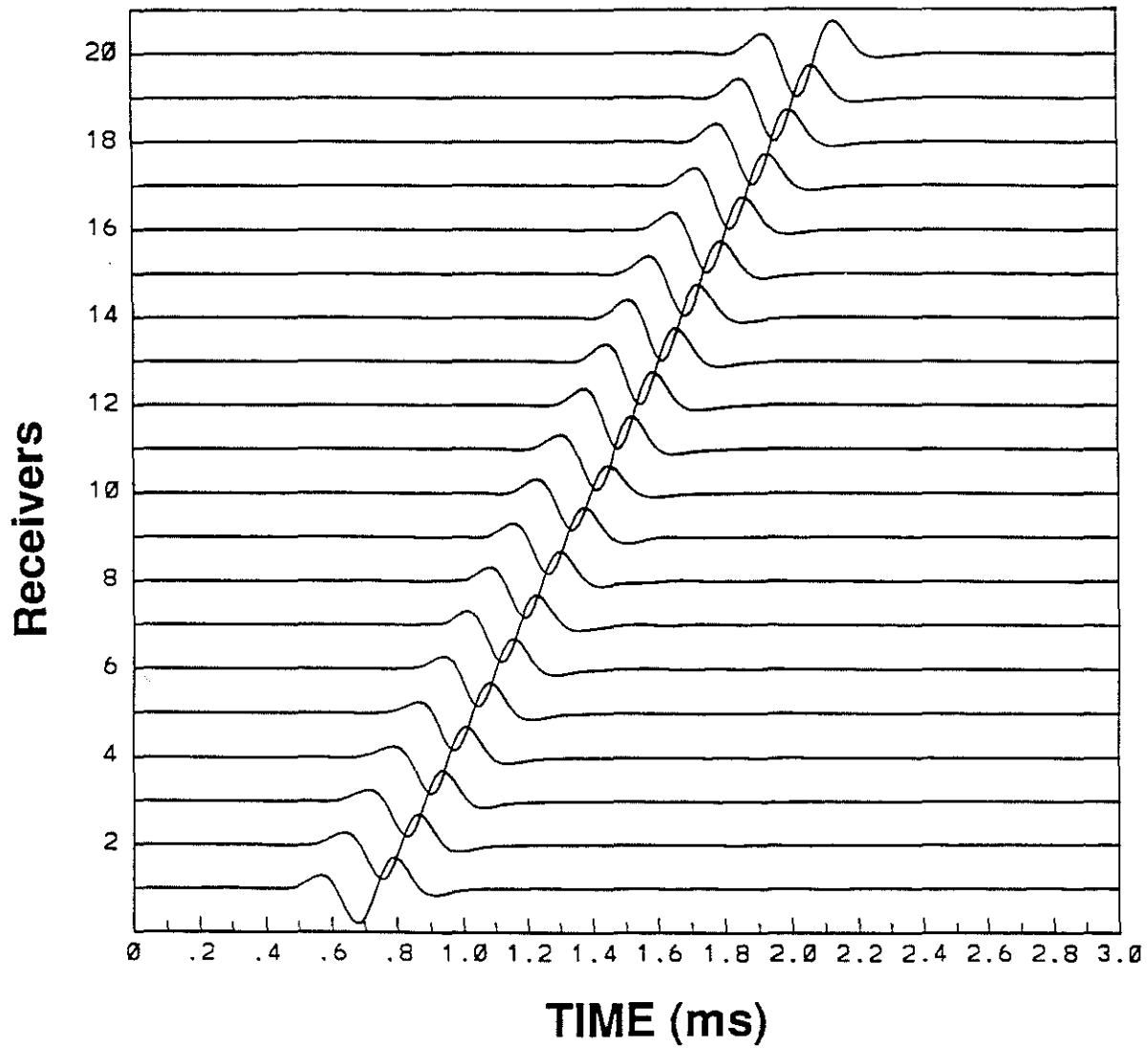
Figure 18: Finite difference synthetics at the center of the borehole with source center frequency at 4 kHz. The receivers start at $z = 1.0$ m and receiver separation is 0.1 m. The layered formation model is used. Layer 1 is Green River shale and layer 2 is Mesaverde limestone. The layer boundary at $z = 2.0$ m.
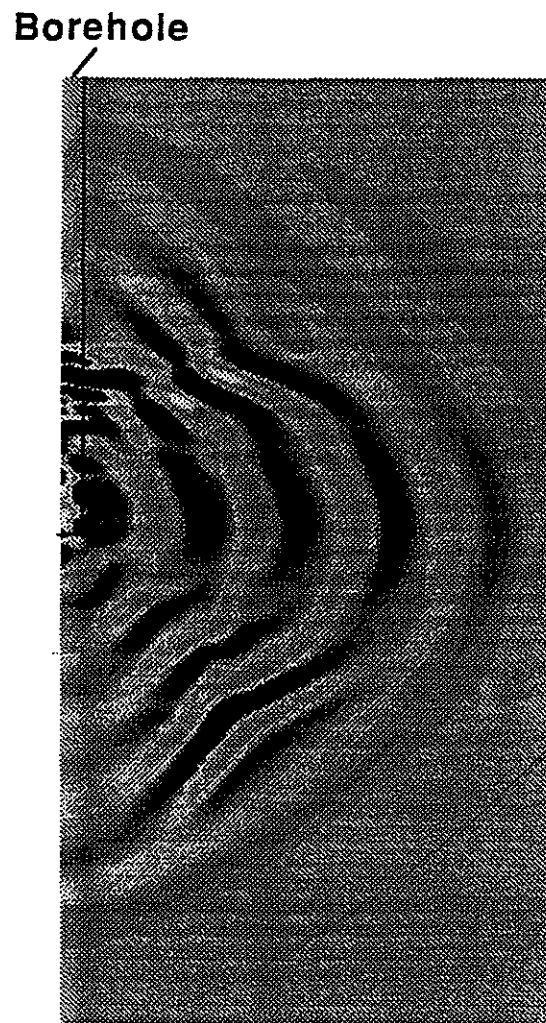
Borehole

Figure 21: Snapshot of wavefield σ_{rr} for the semi-infinite borehole in Green River shale formation at time 0.6 ms.
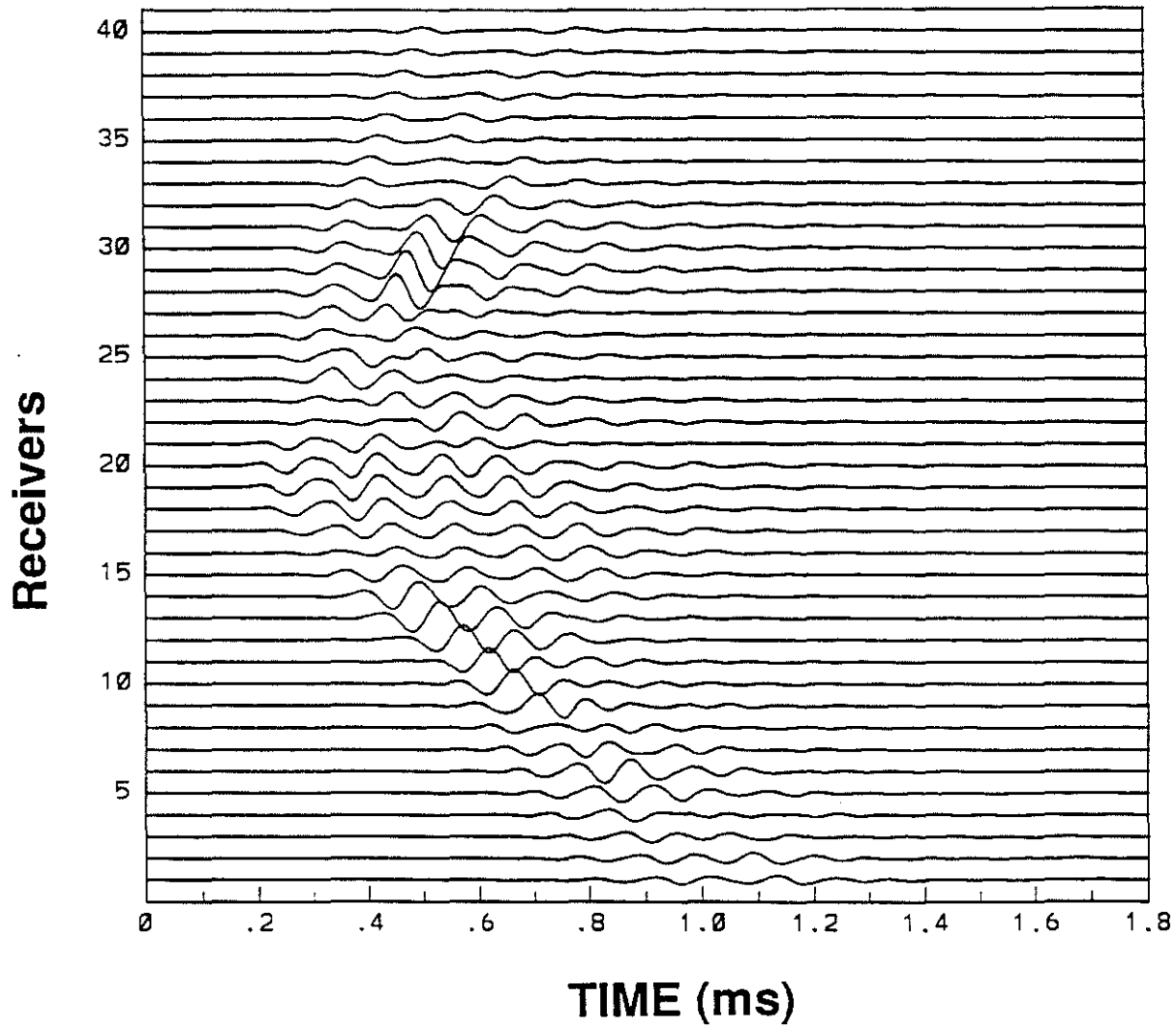
Figure 22: Finite difference synthetics outside the borehole. The fluid-filled borehole ended at $z = 2.5$ m. The formation is Green River shale. The source is a vertical force ring applied at the bottom of the borehole.

Borehole
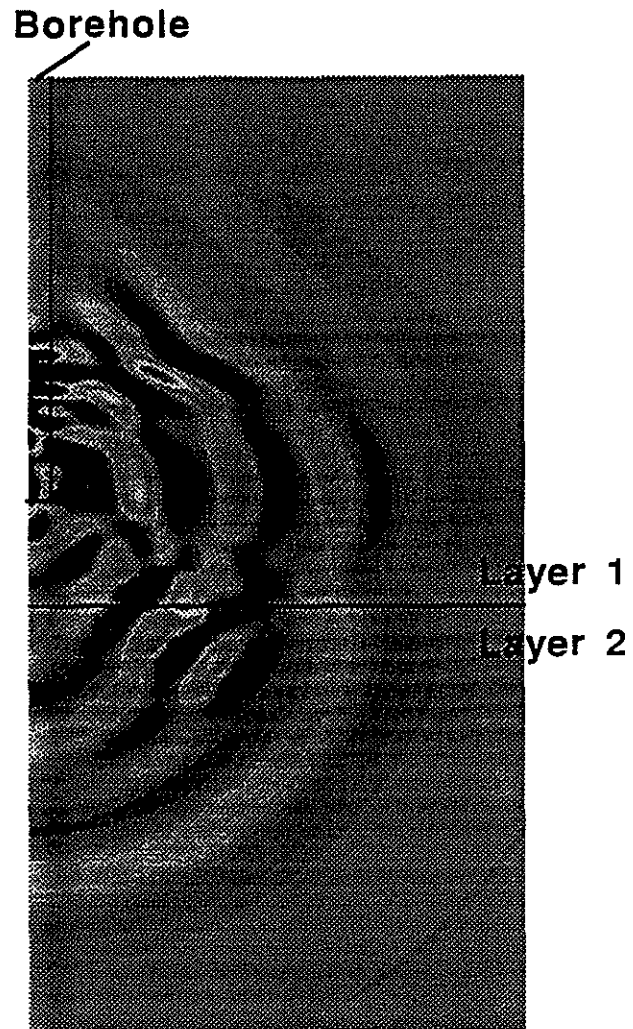

Layer 1

Layer 2

Figure 23: Snapshot of wavefield σ_{rr} for the semi-infinite borehole with layer model at
        time 0.5 ms.